Available online at www.sciencedirect.com
SCIENCE DIRECT
Earth and Planetary Science Letters 248 (2006) 30–42
EPSL
www.elsevier.com/locate/epsl

Mantle temperature variations beneath back-arc spreading centers inferred from seismology, petrology, and bathymetry

Douglas A. Wiens [a,*], Katherine A. Kelley [b,1], Terry Plank [c]

[a] Department of Earth and Planetary Sciences, Washington University, St. Louis, MO, United States
[b] Department of Terrestrial Magnetism, Carnegie Institution of Washington, Washington, DC, United States
[c] Department of Earth Sciences, Boston University, Boston, MA, United States

Received 14 November 2005; received in revised form 2 April 2006; accepted 2 April 2006
Available online 30 June 2006
Editor: R.D. van der Hilst

Abstract

Variations in seismological structure, major element composition, and axial depth between different back-arc spreading centers provide constraints on physical conditions associated with back-arc melt production. We invert vertical and transverse seismograms from several representative paths traversing the Mariana, Lau, North Fiji, and East Scotia back-arc basins. Seismic velocity varies substantially at depths of 40–100 km, with differences of up to 7% between the slowest (Lau) and the fastest (Mariana) structures. These mantle seismological structures correlate with major element systematics and the elevations of the ridge axes, consistent with differences in average upper mantle temperatures. In contrast to the temperature correlation, mantle seismic structure shows no apparent correlation with petrologically inferred water content. Petrological indicators suggest a ~100 °C range in mantle potential temperature, consistent with the seismic velocity variations, assuming experimentally determined temperature derivatives. The temperature variations, however, must extend throughout the upper ~200 km of the mantle wedge to produce the observed ridge elevation differences. Fast slab rollback and the influx of hot Samoan mantle may contribute to high temperatures in the Lau Basin.

Keywords: back-arc basin basalts; upper mantle structure; mantle temperature; Lau Basin; Mariana Trough; major element systematics

1. Introduction

The petrological and geochemical characteristics of back-arc basin basalts vary widely, and show evidence of different extents of partial melting in the mantle [1,2]. Some of this variation is due to different water content provided by subducting slabs, but substantial differences remain even after correcting for the effect of volatiles [3]. The axial elevations of back-arc spreading centers also show large variations. It has previously been unclear whether these differences result from thermal, compositional, or other possible controlling variables. Comparison of upper mantle seismic velocity structures can help to resolve the origin of the observed petrological and bathymetric variations. Several past studies have suggested a link between seismic velocities and major element systematics along the mid-ocean ridge system, but these models used low resolution global models and only found a correlation for depths

* Corresponding author. Tel.: +1 314 935 6517.
E-mail address: doug@wustl.edu (D.A. Wiens).
[1] Now at: Graduate School of Oceanography, University of Rhode Island, Narragansett, RI, United States.

0012-821X/$ - see front matter © 2006 Elsevier B.V. All rights reserved.
doi:10.1016/j.epsl.2006.04.011

greater than 100 km [4,5], much deeper than the zone of primary melt production [6–9]. In addition, the seismic velocity variations found in these prior studies are much smaller than would be expected from the temperature variations inferred from petrology, using experimentally determined velocity–temperature relations [10,11].

2. Regional seismic waveform inversion

We use a regional waveform inversion method [12–16] to determine the average upper mantle shear velocity structure of the Mariana, Lau, North Fiji, and East Scotia back-arc basins. These four regions have large, active back-arc spreading centers, and have the appropriate seismic source and receiver geometries to permit accurate seismic velocity determination using the regional waveform method. An advantage of this method is that it isolates the structure of a particular back-arc basin at a length scale of 500–1000 km without danger of bias due to adjacent regions. Three different source-station geometries are inverted simultaneously to determine the structure of each back-arc region (Table 1). The raypaths sample the back-arc basins broadly and are not confined to the immediate vicinity of the spreading centers (Fig. 1); however, each source-station pair samples back-arc oceanic lithosphere of less than 4 Ma age along nearly the entire raypath.

We invert the entire vertical and transverse regional displacement waveforms extending from the P to the surface wave arrivals to determine the average structure along the path using a niching genetic algorithm inversion [16]. This method finds the SH and SV structures that produce waveform synthetics showing the best fit to the observed data. Inclusion of the entire waveforms ensures that S-wave arrivals and higher mode data are fit, in contrast to typical fundamental-mode surface wave methods, and inclusion of at least one intermediate (100–150 km) depth event for each region gives superior constraints on the deeper part of the model. Synthetics are computed using a standard reflectivity algorithm [17] modified to include an oceanic water layer [13]. The time-domain data misfit is computed in both low-frequency (0.007–0.025 Hz) and higher frequency (0.02–0.07 Hz) bands to ensure both are well fit (Fig. 2).

The structural model consists of a water layer that is set to the average ocean depth along the path, underlain by two crustal layers and upper mantle layers of variable thickness. The thickness of one crustal layer is allowed to vary in order to compensate for different average crustal thickness along the paths. The thickness of upper mantle layers varies from 15 km at shallow depth to 50 km near the 410 km discontinuity, roughly corresponding to the decreasing resolution obtained at depth. Since the synthetics are mostly sensitive to the shear velocity in each layer and we wish to minimize the number of parameters in the inversion, the P-velocity in each layer is tied to the shear velocity by assuming that $d(\ln V_p)/d(\ln V_s)=1.3$ [18,19]. Likewise, the density of each layer is calculated from the P and S velocity by assuming $d\rho/dV_p=80$ kg ms^{-3} km^{-1} [20]. The perturbations in velocity and density are taken relative to the PREM velocity model [21] for the corresponding depth. The attenuation (Q) model was also taken from PREM. The synthetics are only weakly affected by the P velocity, density, and Q model so using different relationships for these quantities will not significantly affect the final result for shear velocity. The synthetics also have limited resolution for the deeper part of the model at these source-station distances, so a linear velocity gradient is assumed at depths between 220 and 410 km, and the PREM velocity model is assumed at depths below 460 km.

Table 1
Earthquakes and seismic stations used in the waveform inversion

Date	Time (GMT) (h/min/s)	Latitude (°N)	Longitude (°E)	Depth (km)	Seismic station	Distance (km)
28-June-1997	16/46/54.5	22.28	142.76	12	Guam	989
14-January-2001	08/58/29.4	22.00	143.77	112	Guam	940
07-April-2001	12/13/27.2	21.67	143.44	15	Guam	909
18-April-2002	14/17/25.8	−60.62	−25.81	13	S. Georgia	951
20-October-2003	16/50/15.8	−58.01	−26.28	116	S. Georgia	756
30-October-2003	06/00/47.3	−60.70	−25.29	10	S. Georgia	977
24-July-1994	17/55/42.0	−16.91	167.65	21	Lautoka, Fiji	1042
22-May-1995	03/45/03.4	−22.67	170.09	13	Lautoka, Fiji	944
29-June-1995	12/24/05.6	−19.33	169.26	144	Lautoka, Fiji	881
12-September-1994	22/43/53.3	−15.31	−173.08	20	Lakeba, Fiji	691
13-November-1995	07/38/44.2	−15.04	−173.43	10	Labasa, Fiji	775
07-December-1999	21/29/49.1	−15.77	−173.95	120	Labasa, Fiji	708

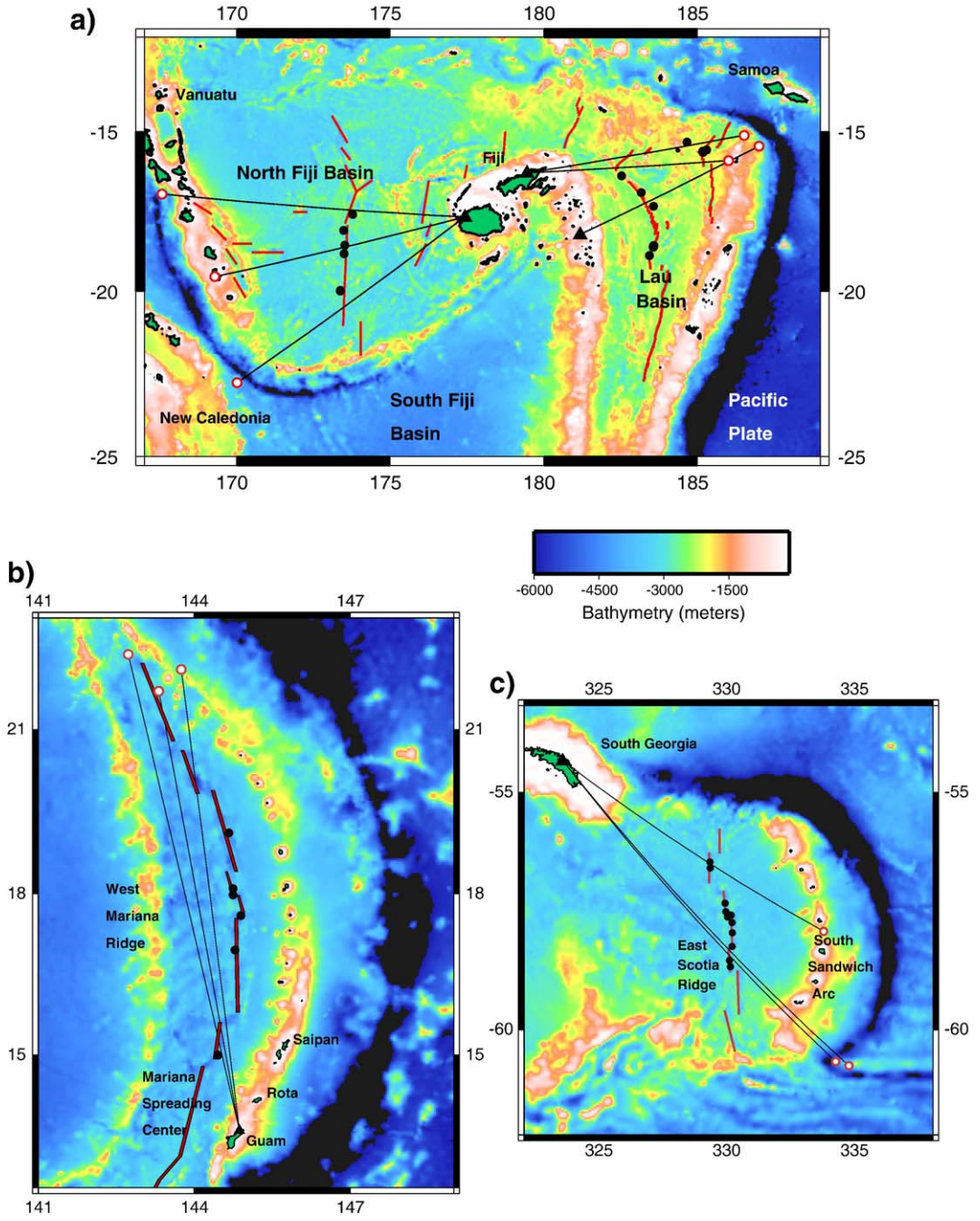

Fig. 1. Bathymetric maps of the a) Lau basin and North Fiji basin, b) the Mariana trough, and c) East Scotia ridge, showing the paths traversed by the seismic waves used in the waveform inversion for structure in each region. Earthquakes used in the inversion are denoted as open circles, seismic stations by filled triangles, basalt sample locations by filled circles, and back-arc spreading centers by red lines.

A niching genetic algorithm is used to optimize the fit between the data and synthetics [22]. This nonlinear optimization procedure is an ensemble approach that begins with a Monte Carlo calculation in the first generation, with ensemble populations of subsequent generations determined by from solutions that maximize the objective function. The inversion is carried out in five different populations, or niches, with a distance metric imposed to prevent convergence, so that several independent favourable solutions may be

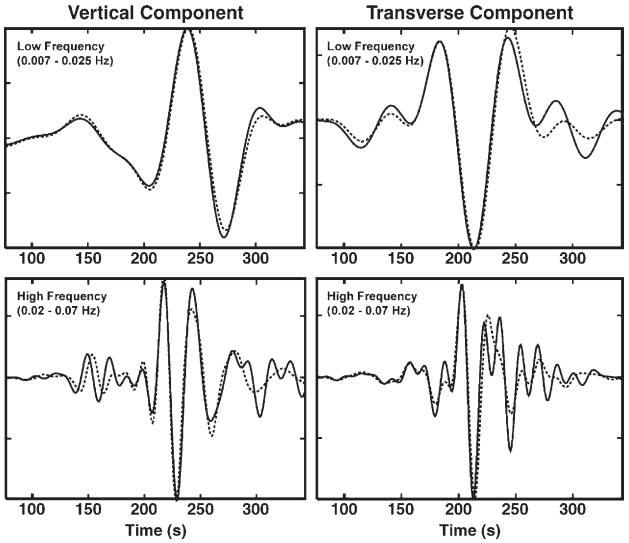

Fig. 2. Observed waveforms (solid lines) and synthetic fits (dotted lines) using the North Fiji Basin structure for the 19-June-1995 event recorded at Lautoka, Fiji (distance 881 km, event depth 144 km).

found if they exist. The objective function is based on the squared error of the time-domain data and synthetics with a smoothing criterion. The transverse (SH) and vertical (SV) components generally cannot be fit by the same velocity structure due to the anisotropy of the uppermost oceanic mantle [23], therefore we allow these structures to differ by 0%–7% between the Moho and 220 km depth. The use of separate SV and SH structures to compute the vertical and transverse synthetics is a good approximation to a truly anisotropic structure in the transversely isotropic case (commonly referred to as polarization anisotropy or radial anisotropy) [16,24]. The crust is assumed to be isotropic, as the dominant lithospheric anisotropy is usually assumed to locate in the upper mantle, but in any case the limited thickness of the oceanic crust (<12 km) yields synthetics with very little sensitivity to crustal anisotropy. A penalty function ensures that any difference between the SH and SV structures is required by the data, thus our solutions show the minimum anisotropy that is compatible with the data. Fig. 3 shows the individual anisotropic structures for each back-arc basin. The four back-arc basins show polarization anisotropy of between 1% and 4% in the uppermost mantle, and the amplitude of the anisotropy generally decreases with depth. Formulas for determining the isotropic structure from the SH and SV velocities generally depend on the symmetry and orientation of the anisotropy [25]; since these parameters are not known for the study regions the isotropic structure is determined by averaging the SH and SV velocities (Fig. 4).

The dispersion of the populations provide some constraints on the uncertainty of the solutions [26,27]. The variance of the model parameters in the population suggests that the resolution for the isotropic structure of all four regions is greatest at depths of 20–60 km and is reduced with increasing depth below this region. The depth distribution and magnitude of the anisotropy is more poorly constrained than the isotropic structure. The presence of strong azimuthal anisotropy would have the potential to bias estimates of the isotropic velocities and radial anisotropy [28]. However, the determination of the isotropic structure from both SV and SH synthetics as done here is much superior to the typical procedure of mapping structure from SV or SH alone. Also the two back-arc basins that have been extensively studied for azimuthal anisotropy using shear wave splitting, the Lau Basin [29] and the Mariana Trough [30], show complex patterns of anisotropic fast directions. Thus back-arc regions do not seem to be characterized by large-scale uniform patterns of seismic anisotropy that might bias regional inversion for isotropic structure.

In this study we investigate the correlation of the averaged isotropic seismic velocity in the low velocity zone (40–100 km depth) with petrological parameters that reflect mantle temperature and water content (Table 2). The uncertainty of this averaged velocity is less than the uncertainty of individual mantle layers, which often trade-off with adjacent layers. We estimate the uncertainty by examining the range of results in the demes (different subpopulations) of the niching genetic algorithm [16,19]. Since each deme represents an

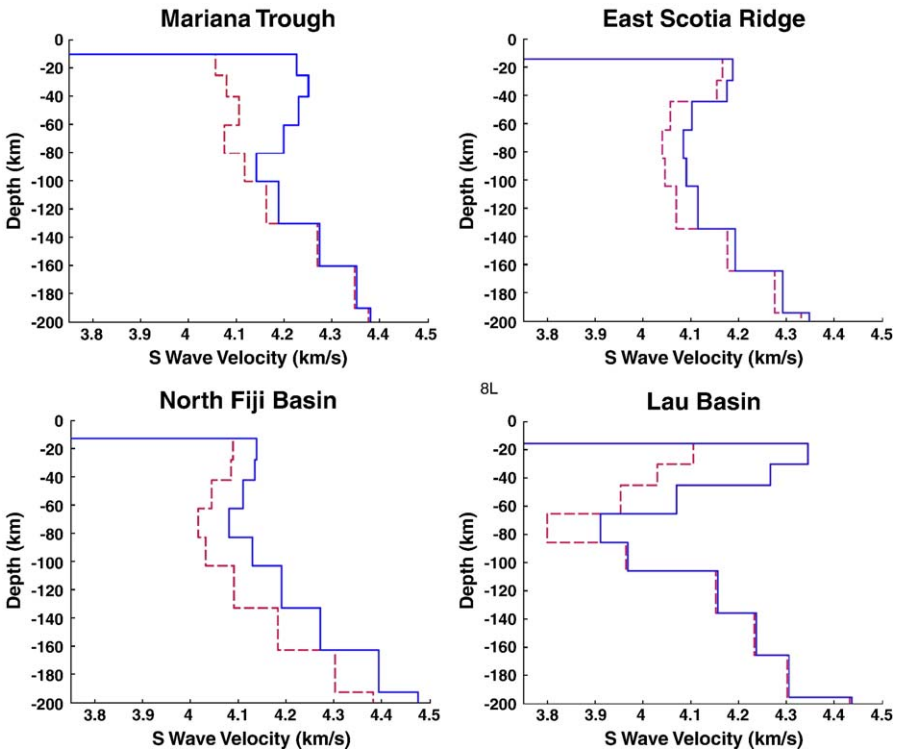

Fig. 3. Waveform inversion results showing the SV (dashed line) and SH (solid line) structures for each region.

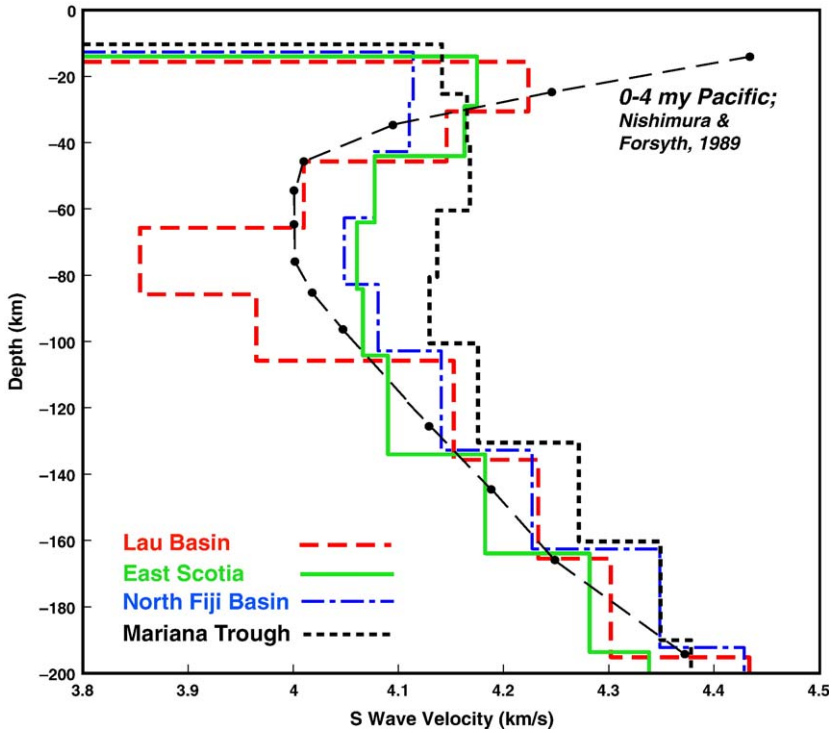

Fig. 4. Isotropic shear wave velocity structure as a function of depth determined from waveform inversion for each of the back-arc regions. The isotropic structure of 0–4 Ma Pacific ocean lithosphere from Nishimura and Forsyth [23] is shown for comparison.

Table 2
Geochemical and seismological data for back-arc basins

Location	Latitude range	Number of samples [a]	$Fe_{(Fo90)}$ concentration [b, c]	$Na_{(Fo90)}$ concentration	Mantle T_p (°C)	Average axial depth [d] (m)	S velocity [e] 40–100 km (km s^{-1})	Mantle H_2O concentration (wt.%) [f]	Basalt H_2O concentration (wt.%) [g]
Marina Trough	15.00°–21.31°N	6 (29)	8.11±0.45	2.71±0.24	1350±12	3918±435	4.145±0.04	0.166±0.04	1.09±0.17 [0.90±0.15]
E. Scotia Ridge	59.17°–56.19°S	11 (35)	8.16±0.11	2.65±0.14	1354±19	3468±192	4.076±0.04	0.075±0.03	0.63±0.21 [0.50±0.17]
N. Fiji Basin	20.43°–16.30°S	6 (6)	9.74±0.35	2.22±0.18	1431±40	2850±184	4.071±0.04	<0.05 [h]	0.45±0.21 [h] [0.35±0.18] [h]
N. Lau Basin	18.88°–15.17°S	16 (34)	9.57±0.25	1.99±0.10	1449±23	2240±236	3.961±0.05	0.056±0.03	0.43±0.14 [0.33±0.12]

[a] Number of samples with H_2O wt.% <0.65 used in the Fe and Na and T_p calculations; parentheses show the number of samples used to calculate average mantle water concentration.
[b] All uncertainties are 2σ values are except as specified.
[c] $Fe_{(Fo90)}$ and $Na_{(Fo90)}$ are compositions corrected for crystal fractionation until in equilibrium with Fo_{90} mantle olivine, as described in the text; equations in Kelley et al. [3].
[d] Axial depth is average along strike depth from the region sampled taken from the ETOPO2 bathymetric database; uncertainties are standard deviations of the axial depth.
[e] Seismic velocity uncertainty taken from the range of best models from the different sub-populations of the niching genetic algorithm.
[f] Mantle H_2O concentration is calculated from all basalts within the study regions (unfiltered for H_2O) using basalt $H_2O_{(Fo90)}$, batch melting, and $TiO_{2(Fo90)}$ as a proxy for melt fraction (see text and Kelley et al. [3]).
[g] Values without brackets are raw glass H_2O data; values in brackets are glass data calculated to $H_2O_{(Fo90)}$ concentrations (see text).
[h] There are no H_2O measurements for samples in the study area; however, H_2O measurements for the rest of the North Fiji indicate melt and mantle H_2O concentrations similar to MORB (mantle $H_2O \leq 0.05$ wt.%).

independent solution providing a locally optimized fit, the range of these values provides a good estimate of the uncertainty of the solution.

3. Major element systematics in back-arc basin basalts

Mantle temperature and H_2O both affect the extents of mantle melting beneath back-arc basins and the resultant compositions of erupted lavas. The major element and volatile compositions of glasses from the four back-arc basins are compiled from: the Mariana Trough [31–39], the Lau Basin [34,40–47], the East Scotia ridge ([48–50] S. Newman, unpublished data) and the North Fiji basin [40,41,51].

We isolate the effect of potential temperature on dry mantle melting by first considering only dry (<0.65 wt. % H_2O) basaltic glasses. This limit minimizes the effect of water on melt composition without decimating the data set (particularly for the Mariana Trough, where all but five sample locations have H_2O=0.72–1.76 wt. %). We take these dry glasses as equivalent to mid-ocean ridge basalts (MORB) in that the primary magmas formed largely by adiabatic decompression. The compositions of these magmas thus relate to the depth and extent of mantle melting, which co-vary as a function of changing mantle potential temperature (T_p). Langmuir et al. ([7]; hereafter, LKP) developed a quantitative model that predicts Na_2O and FeO contents of primary melts generated by adiabatic decompression of mantle of varying T_p. When corrected for low-pressure crystal fractionation to 8 wt.% MgO, LKP showed that the modeled primary melts reproduce well the MORB Na_8–Fe_8 array for fractional melting (their Fig. 53b). Similar results were obtained with an independent method by Kinzler and Grove [8]. The fractionation correction, however, is difficult to perform quantitatively on output from the LKP model, because it does not predict all major element concentrations in the primary melts (only FeO, MgO, Na_2O and TiO_2). We choose instead to back-correct MORB and back-arc basin basalt (BABB) compositions to primary compositions (i.e., in equilibrium with Fo_{90} mantle) to compare directly with the LKP primary melt array.

There are several steps needed to correct basalt glass compositions to those in equilibrium with the mantle. We first filter the dry basalt data to exclude fractionated glasses with <7 wt.% MgO, since the large correction needed for these glasses introduces large uncertainties in the primary compositions. We backtrack BABB with >7% MgO to primary melt concentrations of FeO and Na_2O (i.e., $Fe_{(Fo90)}$ and $Na_{(Fo90)}$) using the approach of Klein and Langmuir [1] to correct back to 8% MgO, and then plagioclase +olivine and olivine only addition to correct to

equilibrium with Fo_{90} mantle olivine (equations given in Kelley et al. [3]).

The $Na_{(Fo90)}$ and $Fe_{(Fo90)}$ compositions calculated in this way can be used to calculate mantle T_p, using the LKP mantle melting model, for fractional melts pooled from the passive upwelling region beneath the spreading center. We parameterize this with the following relationships ($r^2 > 0.99$):

$$T_p(\mathrm{Fe}) = \left[3.4381*(\mathrm{Fe}_{(Fo90)})^2\right] + \left[4.154*\mathrm{Fe}_{(Fo90)}\right] + 1088.6 \quad (1)$$

$$T_p(\mathrm{Na}) = \left[41.164*(\mathrm{Na}_{(Fo90)})^2\right] - \left[336.78*\mathrm{Na}_{(Fo90)}\right] + 1956.1 \quad (2)$$

Averaging T_p(Fe) and T_p(Na) yields quantitative estimates and uncertainties of the mantle T_p beneath mid-ocean ridges and back-arc basins, as reported in Table 2. In rare instances where the difference between the two T_p estimates from a single glass composition was >50 °C, then only T_p(Na) was used in the regional average because the fractionation correction to $Fe_{(Fo90)}$ in high-Fe glasses has greater error than the $Na_{(Fo90)}$ correction.

We averaged the model results of individual glasses from each back-arc basin to establish regional $Na_{(Fo90)}$, $Fe_{(Fo90)}$, and mantle T_p characteristics. Only back-arc basin glasses collected within the regions sampled by the seismic raypaths shown on Fig. 1 were used in these calculations (except in the Lau Basin, see below), but petrological sampling of these regions is not evenly distributed. To avoid biasing the regional averages towards heavily sampled areas, we first averaged all raw glass data from a given sampling location (in most cases a single dredge), and then weighted each location by the appropriate length of ridge axis.

In the Lau Basin, sparse recovery of dry glasses in the relevant regions ($n=4$ with <0.65 wt.% H_2O, all other samples with 0.74–1.31 wt.% H_2O) required us to expand the petrologic database to include glasses from the nearby Central Lau spreading center (CLSC). The calculated temperatures in the CLSC are consistent (within 3%) with constraints from the few dry glasses recovered at the Mangatolou triple junction, the Northern Lau spreading center, and the Peggy ridge, which are all within the region sampled by the seismic raypaths.

To address variations in H_2O content between the four back-arc basins, we also calculate average mantle H_2O concentrations using basalt compositions. We first remove the H_2O concentration filter on the back-arc basalt data set, then use similar composition-dependent fractionation corrections from [3] to calculate the primary melt concentrations of TiO_2 and H_2O (i.e., $TiO_{2(Fo90)}$ and $H_2O_{(Fo90)}$). We then use $TiO_{2(Fo90)}$ and the batch melting equation, as in [3], to determine the melt fraction (F):

$$F = \frac{\left(C^0_{\mathrm{Ti}}/C^1_{\mathrm{Ti}}\right) - D_{\mathrm{Ti}}}{(1 - D_{\mathrm{Ti}})} \quad (3)$$

where C^1_{Ti} is $TiO_{2(Fo90)}$, $D_{\mathrm{Ti}}=0.04$, and C^0_{Ti} is the TiO_2 concentration of the mantle source, as estimated by Kelley et al. [3]. We then rearrange the batch melting equation to constrain the H_2O concentration of the mantle source ($C^0_{H_2O}$):

$$C^0_{H_2O} = C^1_{H_2O}[F(1 - D_{H_2O}) + D_{H_2O}] \quad (4)$$

where $C^1_{H_2O}$ is $H_2O_{(Fo90)}$, $D_{H_2O}=0.012$, and F is from Eq. (3). Average values for the calculated mantle water contents ($C^0_{H_2O}$) are given in Table 2.

4. Correlation between mantle velocity, ridge elevation, and mantle potential temperature

The structure of each of the back-arc basins shows a significant low velocity zone extending from 40 to 100 km depth (Fig. 4), which is slightly deeper than the 30–70 km depth range estimated for the primary MORB melting region based on geochemical considerations [9]. Although the structures of the different back arcs above 40 km and below 100 km are relatively similar, seismic velocities show a large variation within this low velocity zone. The North Fiji Basin and East Scotia back-arcs show seismic velocities similar to that of average 0–4 Ma old East Pacific Rise (EPR) structure [23]. In contrast, the Lau Basin shows seismic velocities that are up to 4.2% lower than the average EPR structure, and the Mariana Trough shows velocities up to 2.7% faster than the EPR structure, with the maximum differences occurring at depths from 65 to 85 km. Recent regional waveform inversion study of the EPR finds SV structures similar to those in this study, and also finds large regional velocity variability at 40–100 km beneath the ridge [15]. Global tomographic models [52,53], although showing significantly higher mantle velocities and lower regional variability for all back-arcs due to limited resolution and smoothing, also find that the Lau and North Fiji basins have lower seismic velocities than the Mariana and East Scotia regions at depths of 40–100 km.

These seismic velocity variations correlate with major element systematics in basalts erupted along the spreading axes as well as with spreading center elevation. For this comparison, we choose basalt samples and tabulate average ridge elevation within the region sampled by the seismic waves, which may extend 100–200 km from the ray path for these epicentral distances (Table 2). Basalts from the region with the highest seismic velocity and the lowest elevation, the Mariana Trough, have the highest $Na_{(Fo90)}$, while basalts from the region with the lowest seismic velocity and the highest elevation, the Lau Basin, have the lowest $Na_{(Fo90)}$ (Fig. 5a). These variations mirror those seen globally in mid-ocean ridge basalts (MORBs), and indeed, major element compositions of the driest basalts (i.e., <0.65 wt.% H_2O) from back-arc basins fall within the global array of MORB (Fig. 5b). Although source heterogeneity and melting dynamics are important regional factors [9], the full magnitude of global Na_2O and FeO variations in MORB are best described quantitatively by variations in mantle potential temperature (T_p), which determines both the depth where melting initiates and the mean and maximum extent of melting [6–9,54]. High T_p causes greater initial depth of melting (which leads to high $Fe_{(Fo90)}$) and greater mean extents of melting (which leads to low $Na_{(Fo90)}$). These systematics, developed for MORB, should also apply to the driest back-arc basin basalts, given their compositional similarities (Fig 5b). Water locally drives additional melting beneath back-arc basins [38], but the baseline variations from region to region are most consistent with mantle T_p variations [3]. For the back-arc regions of interest here, mantle T_p (calculated from Na and Fe) varies by about 100 °C (Table 2), with the Mariana Trough as the coolest (T_p=1350± 12 °C) and the northern Lau Basin as the hottest (T_p=1449±20 °C).

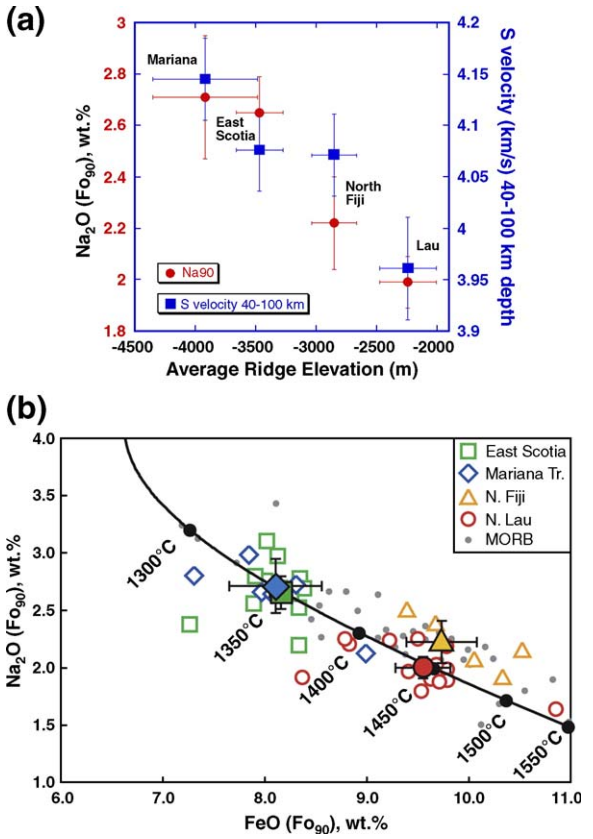

Fig. 5. (a) Correlation between seismic velocity (squares), average ridge depth, and $Na_{(Fo90)}$ concentration (circles) for the different back-arc basins. The average S velocity between 40 and 100 km depth and Na_2O concentration in equilibrium with Fo_{90} are plotted as a function of average ridge depth (values given in Table 2). (b) Na_2O vs. FeO in mid-ocean ridge and back-arc basin basalts, corrected to equilibrium with Fo_{90} olivine. Solid black line is model curve of primary mantle melts (accumulated, pooled fractional melts) from Langmuir et al. [7], black circles on this curve mark mantle T_p. Open symbols show individual back-arc basalt data points, large filled symbols are regional back-arc basin averages. MORB data are from Klein and Langmuir [1], and references therein, BABB data are referenced in the text.

5. Discussion

5.1. The possible effect of water

The petrological data suggest that the seismic velocity and ridge elevation variations may be caused in large part by regional differences in mantle temperature. In contrast, the observed trends cannot be due to variations in mantle wedge water content, since the trends do not show the expected reduction in seismic velocity with increased water [55]. For example, the mantle beneath the Mariana Trough has the highest average water content, yet also the highest seismic velocities (Table 2), exactly opposite to the relationship expected from water alone. Thus the effect of temperature on seismic velocity seems to dominate the effect of water in the back-arc basins.

This observation is consistent with what is known about the effect of water on seismic velocities and the average water content of the upper mantle in the back-arc regions inferred from petrology (Table 2) [3]. Olivine can store up to 0.08 wt.% of water at a depth of 100 km in its crystal structure [56,57]. The average water contents of three of the back-arc regions are less than this value, but the Mariana Trough shows a value greater than the storage capacity of olivine (0.166 wt. %). Recent studies suggest that pyroxene can store significant water in the upper mantle and that the total

storage capacity may be greater than 0.2 wt.% at 100 km depth. Thus the inferred average water contents of the back-arc regions can largely be accommodated in the crystal structures of upper mantle minerals without the formation of a free hydrous phase at 100 km, although the full range of water contents in back-arc basalts requires that localized regions may exceed the minimum storage capacity [3]. At shallower depths the water storage capacity is further reduced and water is involved in the formation of hydrous melts; the possible effect of melt on seismic velocity is discussed in the next section.

Discussion of the seismic effects of water in the upper mantle involves some assumptions, since published relations assume water is stored in pure olivine [55]. However, assuming that the seismic effects of upper mantle peridotite are similar to olivine, increasing the upper mantle water content from normal MORB (0.005 wt.%) to the average water content of the Mariana back-arc (0.166 wt.%) will reduce the shear velocity by about 1.5%. This is clearly much less than the observed maximum variation of 7% at depths of 60–80 km or even the 4.5% variation in the average velocity at 40–100 km depth. Although some of the observed trends in the data may be influenced by water content, such as the high mantle velocities of the dry North Fiji Basin relative to the trend of the other back-arcs (Fig. 6a), our observation that the velocity variations are dominated by temperature and not water content is consistent with available data.

5.2. The relative variation of mantle temperature and seismic velocity

The amplitude of the inferred temperature differences is generally consistent with the observed variations in seismic velocity and ridge elevation. Fig. 6a plots the average seismic velocity between 40 and 100 km depth as a function of T_p as determined from the major element systematics. A linear regression through this data gives a slope of 1.2 ms^{-1} $°C^{-1}$, and a larger slope (~1.8 ms^{-1} $°C^{-1}$) is suggested using only the Lau and Mariana end points. Both of these values are larger than previous experimental ultrasonic determinations of the derivative of velocity with respect to temperature [18,58] and are nearly an order of magnitude larger than the values of 0.20 ms^{-1} $°C^{-1}$ suggested by previous seismic velocity and MORB geochemistry correlations [4]. Recent experiments at seismic frequencies including both elastic and inelastic effects, however, suggest that the velocity derivative is in the range of 1.0 to 2.0 ms^{-1} $°C^{-1}$ at temperatures of 1350 °C and typical upper mantle grain sizes of 1–10 mm [11,59]. The observed seismic velocity variations are therefore consistent with the petrologically constrained temperature range of 100 °C between these back-arc basins.

While the observed seismic velocity variation between different back arcs may be due entirely to temperature, upper mantle melt content could also affect seismic velocities. Estimates of mantle melt porosity beneath spreading centers range from nearly

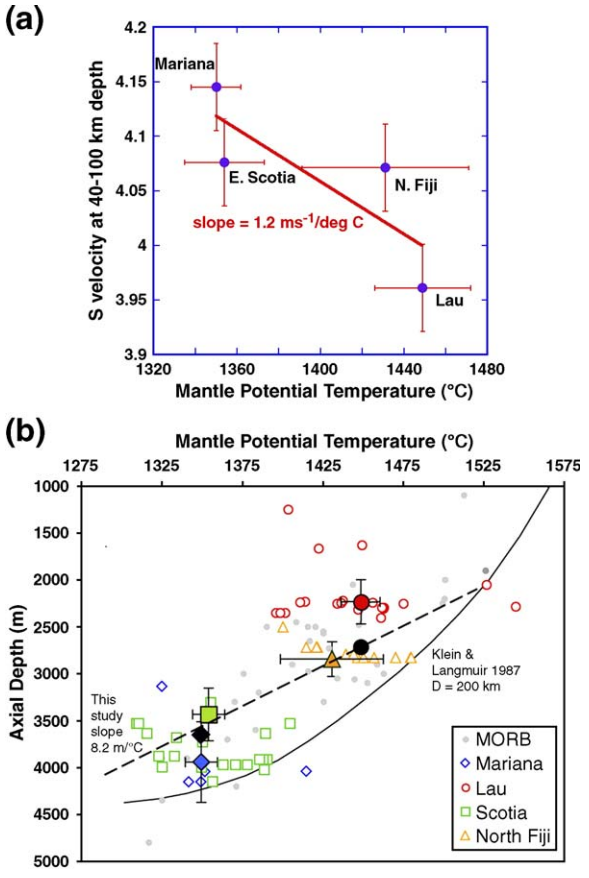

Fig. 6. (a) Correlation of average shear wave velocity from 40 to 100 km depth with the mantle potential temperature determined from major element systematics. Line denotes the least squares fit. Slope provides estimate of temperature derivative of seismic velocity assuming the seismic velocity variations result entirely from temperature. (b) Mantle T_p vs. ridge axial depth for mid-ocean ridges and back-arc basins. Small open symbols without error bars are individual samples, large filled symbols with error bars are weighted averages for each of the back-arc basins, and large black symbols are Mariana and Lau ridge elevations corrected for crustal thickness and the buoyancy of the depleted mantle. MORB data are from [1] and references therein, BABB data are referenced in the text, and T_p is calculated as described in the text. Dashed line is least squares fit to the corrected average back-arc data, and the solid line is the modeled ridge depths as a function of mantle temperature for a compensation depth of 200 km from Klein and Langmuir [1].

zero [60,61] to greater than 1% [62,63]. If significant melt porosity exists in the upper mantle, then some of the observed seismic velocity variation observed at depths of 40–100 km may result from variations in melt content, since melt has a dramatic effect on seismic velocity [59], and these depths represent the primary melting region. In this case, warmer back-arcs may exhibit greater melt content that produces larger velocity reductions. The amplitude of the observed seismic velocity variation is, however, consistent with the petrologically modelled temperature variations without the additional effect of melt porosity.

Fig. 6b shows a strong correlation between ridge elevation and mantle potential temperature constrained by petrology. The back-arc basin results plot well within the MORB temperature–depth range, suggesting processes unique to back-arc basins such as higher water contents have limited effect on axial depth (although other, wetter, back-arc regions, such as the southern Lau Basin, may show more of an effect [3]). Klein and Langmuir [1] ascribed the relationship between ridge elevation and mantle temperature to the combined effect of extra crustal thickness, buoyancy of the residual upper mantle, and thermal buoyancy of the upper mantle. In situ melt buoyancy is insufficient to produce a significant effect on the ridge elevation for reasonable values of melt porosity (~1%).

5.3. Estimated depth extent of the temperature differences

We can use observed crustal thickness, and the predicted effect on mantle residuum buoyancy, to determine the relative contribution of various factors in the observed axial depth variations, and thus place constraints on the magnitude of upper mantle thermal buoyancy. Seismic refraction and gravity studies show a crustal thickness of 7.5 km for the Lau Basin near the Central Lau spreading center [64] and about 5 km for average crustal thickness near the Mariana spreading center [65,66]. Reliable crustal thicknesses for the North Fiji basin and the East Scotia ridge have not been published, although preliminary analysis of East Scotia data suggests a crustal thickness of approximately 6 km [67]. A simple isostatic calculation shows that these thicknesses should produce an elevation excess of 390 m for the Lau Basin and an elevation deficit of 260 m for the Mariana spreading center, relative to an average upper mantle crustal thickness of 6 km. The buoyancy effect of the mantle residuum resulting from melt production for crustal formation is 30% of the effect from crustal thickness variation [1], so including the effect of depleted upper mantle buoyancy changes these values to +510 and −340 m, respectively. These elevation variations are much smaller than the observed variation in ridge elevation, which are greater than 1600 m, and thus suggest that thermal buoyancy in the mantle accounts for about one-half of the observed large-scale variation in axial depth.

The observed slope from the plot of ridge elevation corrected for crustal thickness as a function of mantle potential temperature (Fig. 6b) provides an estimate of the thickness of the layer in which temperature varies. Simple isostacy gives:

$$Z_T = (\Delta Z/\Delta T)(\rho_m - \rho_w)/\alpha\rho_m \quad (15)$$

where Z_T is the thickness of the perturbed layer, α is the volume coefficient of thermal expansion (3×10^{-5} °C^{-1}); $\Delta Z/\Delta T$ is the rate at which the ridge elevation varies as a function of mantle temperature after correction for crustal thickness and mantle depletion (as above), and ρ_m and ρ_w are the densities of the mantle and the ocean, respectively. The observed $\Delta Z/\Delta T$ of 8.2 m °C^{-1} from Fig. 6b provides an estimate of ~190 km for the thickness of the layer in which the temperature varies beneath the ridges of the different back-arcs. This result is similar to the compensation depths of 150–200 km estimated for mid-ocean ridges by Klein and Langmuir [1] (Fig. 6b).

The amplitude of the elevation difference between the various back arcs suggests that the temperature differences extend through approximately 200 km of the mantle wedge. The seismic structures of the four back-arc regions, however, do not show resolvable differences at depths greater than 110 km (Fig. 4). One explanation for the lack of difference below 110 km is the reduction in both seismic resolution and the temperature derivative below this depth. Seismic resolution from the regional waveform technique is greatest at depths of 20–60 km and decreases for greater depths; with resolution at 200 km depth a factor of 2–3 times less than in the uppermost mantle. In addition, the temperature derivative of seismic velocity decreases by about 33% between depths of 50 and 200 km using an activation volume formula [11], reducing the seismic velocity variations expected for a given temperature variation. Alternatively, the reduction in velocity heterogeneity between the different back arcs at depths greater than 110 km may represent the lower extent of the melting zone if upper mantle porosity is significant and if some of the velocity differences are produced by variations in upper mantle melt content.

6. Implications

We have shown that large-scale variations in petrological and geochemical characteristics of back-arc basins are correlated with seismic velocity variations, and that these variations result from ~100 °C variations in mantle temperature. These variations imply significant differences in the mantle dynamics of the four regions studied here.

The differences in back-arc mantle temperature may result from the particular pattern and vigor of mantle flow in the four regions studied. The temperatures of the four regions seem to reflect the integrated spreading rate of the back-arc spreading centers in each of the regions, with Lau showing the fastest spreading rates and Mariana the slowest. The Lau region is also characterized by extremely rapid subduction (i.e., up to 240 mm/yr [68]), slab rollback, and mantle inflow from the Samoa hotspot region to the north [69,70]. Mantle flow models suggest that rapid back-arc spreading, rapid plate convergence, and slab rollback drive more vigorous flow in the mantle wedge. These regions show warmer wedge temperatures due to the influx of mantle material that has not been cooled by prolonged proximity to the cold subducting slab [71,72]. Thus subducting slabs that are relatively stationary in the mantle such as Mariana may correspond to relatively cool mantle wedge temperatures, and slabs characterized by rapid slab rollback such as the Tonga–Lau system may lead to higher wedge temperatures and more vigorous mantle flow patterns.

Acknowledgements

This research was supported by National Science Foundation MARGINS program grants to DAW and TP and a Carnegie Postdoctoral Fellowship to KK. Seismic data were obtained from the Data Management Center of the Incorporated Research Institutions in Seismology (IRIS). We thank Charlie Langmuir for use of his melting models, James Conder and Uli Faul for helpful comments, and Suzan Van der Lee and Stephan Sobolev for reviews.

References

[1] E.M. Klein, C.H. Langmuir, Global correlations of ocean ridge basalt chemistry and axial depth and crustal thickness, J. Geophys. Res. 92 (1987) 8089–8115.
[2] B. Taylor, F. Martinez, Back-arc basin basalt systematics, Earth Planet. Sci. Lett. 210 (2003) 481–497.
[3] K.A. Kelley, T. Plank, T.L. Grove, E.M. Stolper, S. Newman, E. Hauri, Mantle melting as a function of water content beneath back-arc basins, J. Geophys. Res. (in press).
[4] E. Humler, J.L. Thirot, J.P. Montagner, Global correlations of mid-ocean-ridge basalt chemistry with seismic tomographic images, Nature 364 (1993) 225–228.
[5] S. Zhang, T. Tanimoto, E.M. Stolper, S-wave velocity, basalt chemistry, and bathymetry along the Mid-Atlantic Ridge, Phys. Earth Planet. Inter. 84 (1994) 79–93.
[6] D. McKenzie, M.J. Bickle, The volume and composition of melt generated by extension of the lithosphere, J. Petrol. 29 (1988) 625–679.
[7] C. Langmuir, E.M. Klein, T. Plank, Petrological systematics of mid-ocean ridge basalts: constraints on melt generation beneath ocean ridges, Mantle Flow and Melt Generation at Mid-Ocean Ridges, American Geophysical Union, Washington, DC, 1992, pp. 183–280.
[8] R.J. Kinzler, T.L. Grove, Primary magmas of midocean ridge basalts: 2. Applications, J. Geophys. Res. 97 (1992) 6907–6926.
[9] Y. Shen, D.W. Forsyth, Geochemical constraints on initial and final depths of melting beneath mid-ocean ridges, J. Geophys. Res. 100 (1995) 2211–2238.
[10] I. Jackson, J.D. Fitz Gerald, U.H. Faul, B.H. Tan, Grain-size-sensitive seismic wave attenuation in polycrystaline olivine, J. Geophys. Res. 107 (2002), doi:10.1029/2001JB001225.
[11] U.H. Faul, I. Jackson, The seismological signature of temperature and grain size variations in the upper mantle, Earth Planet. Sci. Lett. 234 (2005) 119–134.
[12] A. Zielhuis, G. Nolet, Shear-wave velocity variations in the upper mantle beneath central Europe, Geophys. J. Int. 117 (1995) 695–715.
[13] Y. Xu, D.A. Wiens, Upper mantle structure of the Southwest Pacific from regional waveform inversion, J. Geophys. Res. 102 (1997) 27439–27451.
[14] F. Marone, S. van der Lee, D. Giardini, Three-dimensional upper-mantle S-velocity model for the Eurasia–Africa plate boundary region, Geophys. J. Int. 158 (2004) 109–130.
[15] Y.J. Gu, S.C. Webb, A. Lerner-Lam, J.B. Gaherty, Upper mantle structure beneath the Eastern Pacific Ocean Ridges, J. Geophys. Res. 110 (2005) B06305, doi:10.1029/2004JB003381.
[16] S.D.R. Maurice, D.A. Wiens, K. Koper, E. Vera, Crustal and upper mantle structure of southernmost South America inferred from regional waveform inversion, J. Geophys. Res. 108 (2003), doi:10.1029/2002JB001828.
[17] B.L.N. Kennett, Seismic Wave Propagation in Stratified Media, Cambridge University Press, Cambridge, 1983, 339 pp.
[18] O.L. Anderson, D. Isaak, H. Oda, High-temperature elastic constant data on mineral relevant to geophysics, Rev. Geophys. 30 (1992) 57–90.
[19] K.D. Koper, D.A. Wiens, L.M. Dorman, J.A. Hildebrand, S.C. Webb, Constraints on the origin of slab and mantle wedge anomalies in Tonga from the ratio of S to P anomalies, J. Geophys. Res. 104 (1999) 15089–15104.
[20] D. Ravat, Z. Lu, L.W. Braile, Velocity–density relationships and modeling the lithospheric variations of the Kenya Rift, Tectonophysics 302 (1999) 225–240.
[21] A.M. Dziewonski, D.L. Anderson, Preliminary reference Earth model, Phys. Earth Planet. Inter. 25 (1981) 297–356.
[22] K. Koper, D.A. Wiens, M.E. Wysession, Multimodal function optimization with a niching genetic algorithm: a seismological example, Bull. Seismol. Soc. Am. 89 (1999) 978–988.

[23] C. Nishimura, D.W. Forsyth, The anisotropic structure of the upper mantle in the Pacific Ocean, Geophys. J. 96 (1989) 203–229.
[24] S.C. Webb, D.W. Forsyth, Structure of the upper mantle under the EPR from waveform inversion of regional events, Science 280 (1998) 1227–1229.
[25] V. Babuska, M. Cara, Seismic Anisotropy in the Earth, Kluwer, Dordrecht, Netherlands, 1991, 213 pp.
[26] H. Douma, R. Snieder, A. Lomax, Ensemble inference in terms of empirical orthogonal functions, Geophys. J. Int. 127 (1996) 363–378.
[27] M. Sambridge, Geophysical inversion with a neighborhood algorithm: I. Searching a parameter space, Geophys. J. Int. 138 (1999) 479–494.
[28] E.W.F. Larson, J. Tromp, G. Ekstrom, Effects of slight anisotropy on surface waves, Geophys. J. Int. 132 (1998) 654–666.
[29] G.P. Smith, D.A. Wiens, K.M. Fischer, L.M. Dorman, S.C. Webb, J.A. Hildebrand, A complex pattern of mantle flow in the Lau backarc, Science 292 (2001) 713–716.
[30] S.H. Pozgay, D.A. Wiens, H. Shoibara, H. Sugoika, Seismic anisotropy and mantle flow across the Mariana Subduction System, EOS Trans.-Am. Geophys. Union 86 (Fall Meet. Suppl.) (2005) Abstract T53A-1411.
[31] G. Fine, E.M. Stolper, The speciation of carbon dioxide in sodium aluminosilicate glasses, Contrib. Mineral. Petrol. 91 (1985) 105–121.
[32] R.F. Gribble, R.J. Stern, S.H. Bloomer, D. Stuben, T. O'Hearn, S. Newman, MORB mantle and subduction components interact to generate basalts in the southern Mariana Trough back-arc basin, Geochim. Cosmochim. Acta 60 (1996) 2153–2166.
[33] R.F. Gribble, R.J. Stern, S. Newman, S.H. Bloomer, T. O'Hearn, Chemical and isotopic compositions of lavas from the Northern Mariana Trough: implications for Magmagenesis in Back-arc basins, J. Petrol. 39 (1998) 125–154.
[34] J.W. Hawkins, J.T. Melchior, Petrology of Mariana Trough and Lau Basin basalts, J. Geophys. Res. 90 (1985) 11,431–411,468.
[35] J.W. Hawkins, P.F. Lonsdale, J.D. Macdougall, A.M. Volpe, Petrology of the axial ridge of the Mariana Trench backarc spreading center, Earth Planet. Sci. Lett. 100 (1990) 226–250.
[36] S. Newman, E. Stolper, R.J. Stern, H_2O and CO_2 in magmas from the Mariana arc and back-arc systems, Geochem. Geophys. Geosyst. 1 (2000).
[37] R. Poreda, Helium-3 and deuterium in backarc basin basalts: Lau Basin and Mariana Trough, Earth Planet. Sci. Lett. 76 (1985) 244–254.
[38] E. Stolper, S. Newman, The role of water in the petrogenesis of the Mariana Trough magmas, Earth Planet. Sci. Lett. 121 (1994) 293–325.
[39] A.M. Volpe, J.D. Macdougall, J.W. Hawkins, Mariana Trough basalts (MTB): trace element ad Sr–Nd isotopic evidence for mixing between MORB-like and arc-like melts, Earth Planet. Sci. Lett. 82 (1987) 241–254.
[40] K.E. Aggrey, D.W. Muenow, J.M. Sinton, Volatile abundances in submarine glasses from the North Fiji and Lau back-arc basins, Geochim. Cosmochim. Acta 52 (1988) 2501–2506.
[41] L.V. Danyushevsky, T.J. Falloon, A.V. Sobolov, A.J. Crawford, M. Carroll, R.C. Price, The H_2O content of basalt glasses from Southwest Pacific back-arc basins, Earth Planet. Sci. Lett. 117 (1993) 347–362.
[42] A. Jambon, J.L. Zimmermann, Water in oceanic basalts: evidence for dehydration of recycled crust, Earth Planet. Sci. Lett. 101 (1990) 323–331.
[43] A.J.R. Kent, D.W. Peate, S. Newman, E. Stolper, J.A. Pearce, Chlorine in submarine glasses from the Lau Basin: seawater contamination and constraints on the composition of slab-derived fluids, Earth Planet. Sci. Lett. 202 (2002) 361–377.
[44] S. Newman (unpublished data).
[45] D.W. Peate, T.F. Kokfelt, C.J. Hawkesworth, J.M. P.W.v. Clasteren, J.A. Hergt, U-series isotope data on Lau Basin glasses: the role of subduction-related fluids during melt migration in back-arc basins, J. Petrol. 42 (2001) 1449–1470.
[46] J.M. Sinton, R.C. Price, K.T.M. Johnson, H. Staudigel, A. Zindler, Petrology and geochemistry of submarine lavas from the Lau and North Fiji backarc basins, in: L.W. Kroenke, J.V. Eads (Eds.), Basin Formation, Ridge Crest Processes and Metallogenesis in the North Fiji Basin, Circum-Pacific Council for Energy and Mineral Resources Earth Sceince Series, vol. 15, 1993, pp. 119–135.
[47] G. Sunkel, Origin of petrological and geochemical variations of Lau Basin lavas (SW Pacific), Mar. Min. 9 (1990) 205–234.
[48] S. Fretzdorff, R.A. Livermore, C.W. Devey, P.T. Leat, P. Sotffers, Petrogenesis of the back-arc East Scotia Ridge, South Atlantic Ocean, J. Petrol. 43 (2002) 1435–1467.
[49] P.T. Leat, R.A. Livermore, I.L. Millar, J.A. Pearce, Magma supply in back-arc spreading centre segment E2, East Scotia Ridge, J. Petrol. 41 (2000) 845–866.
[50] D.W. Muenow, N.W.K. Liu, M.O. Garcia, A.D. Saunders, Volatiles in submarine volcanic rocks from the spreading axis of the East Scotia Sea back-arc basin, Earth Planet. Sci. Lett. 47 (1980) 149–153.
[51] J.-P. Eissen, C. Lefèvre, P. Maillet, G. Morvan, M. Nohara, Petrology and geochemistry of the central North Fiji Basin spreading centre (Southwest Pacific) between 16°S and 22°S, Mar. Geol. 98 (1991) 201–239.
[52] C. Megnin, B. Romanowicz, The three-dimensional shear velocity structure of the mantle from the inversion of body, surface, and higher-mode waveforms, Geophys. J. Int. 143 (2000) 709–728.
[53] M.H. Ritzwoller, N.M. Shapiro, M.P. Barmin, A.L. Levshin, Global surface wave diffraction tomography, J. Geophys. Res. 107 (2002) 2335.
[54] P.D. Asimow, M.M. Hirschmann, E.M. Stolper, Calculation of peridotite partial melting from thermodynamic models of minerals and melts: IV. Adiabatic decompression and the composition and mean properties of mid-ocean ridge basalts, J. Petrol. 42 (2001) 963–998.
[55] S.-I. Karato, Mapping water content in the upper mantle, in: J.M. Eiler (Ed.), Inside the Subduction Factory, Geophysical Monograph, vol. 138, American Geophysical Union, Washington, DC, 2003, pp. 135–152.
[56] G. Hirth, D. Kohlstedt, Water in the oceanic upper mantle: implications for rheology, melt extraction and the evolution of the lithosphere, Earth Planet. Sci. Lett. 144 (1996) 93–108.
[57] M.M. Hirschmann, C. Aubaud, A.C. Withers, Storage capacity of H_2O in nominally anhydrous minerals in the upper mantle, Earth Planet. Sci. Lett. 236 (2005) 167–181.
[58] D.G. Isaak, High-temperature elasticity of iron-bearing olivines, J. Geophys. Res. 97 (1992) 1871–1885.
[59] U.H. Faul, J.D. Fitz Gerald, I. Jackson, Shear wave attenuation and dispersion in melt-bearing olivine crystals: 2. Microstructural interpretation and seismological implications, J. Geophys. Res. 109 (2004), doi:10.1029/2003JB002407.
[60] M. Spiegelman, T. Elliott, Consequences of melt transport for uranium series disequilibrium in young lavas, Earth Planet. Sci. Lett. 118 (1993) 1–20.

[61] C.C. Lundstrom, J. Gill, Q. Williams, Investigating solid mantle upwelling beneath mid-ocean ridges using U-series disequilibria: I. A global approach, Earth Planet. Sci. Lett. 157 (1998) 151–165.
[62] U.H. Faul, Melt retention and segregation beneath mid-ocean ridges, Nature 410 (2001) 920–923.
[63] W.C. Hammond, D.R. Toomey, Seismic velocity anisotropy and heterogeneity beneath the Mantle Electromagnetic and Tomography Experiment (MELT) region of the East Pacific Rise from analysis of P and S body waves, J. Geophys. Res. 108 (2003) 2176, doi:10.1029/2002JB001789.
[64] W.C. Crawford, J.A. Hildebrand, L.M. Dorman, S.C. Webb, D.A. Wiens, Tonga Ridge and Lau Basin crustal structure from seismic refraction data, J. Geophys. Res. 108 (2003), doi:10.1029/2001JB001435.
[65] N. Takahashi, Y. Kaiho, T. Sato, G. Fujie, S. Kodaira, Y. Kanada, Crustal growth of the Izu–Ogasawaran–Mariana Ocean Island Arc inferred from seismic velocity structures, EOS Trans AGU 86 (Fall Meet. Suppl.) (2005) Abstract T53-1408.
[66] K. Kitada, N. Seama, T. Yamazaki, Y. Nogi, K. Suyehiro, Distinct regional differences in crustal thickness along the axis of the Mariana Trough, inferred from gravity anomalies, Geochem. Geophys. Geosyst. 7 (2006) Q04011, doi:10.1029/2005GC001119.
[67] R. Larter, unpublished data, 2005.
[68] M. Bevis, et al., Geodetic observations of very rapid convergence and back-arc extension at the Tonga arc, Nature 374 (1995) 249–251.
[69] S. Turner, C. Hawkesworth, Using geochemistry to map mantle flow beneath the Lau Basin, Geology 26 (1998) 1019–1022.
[70] G.P. Smith, D.A. Wiens, K.M. Fischer, L.M. Dorman, S.C. Webb, J.A. Hildebrand, A complex pattern of mantle flow in the Lau backarc, Science 292 (2001) 713–716.
[71] C. Kincaid, P.S. Hall, Role of back arc spreading in circulation and melting at subduction zones, J. Geophys. Res. 108 (2003), doi:10.1029/2001JB001174.
[72] C. Kincaid, R.W. Griffiths, Laboratory models of the thermal evolution of the mantle during rollback subduction, Nature 425 (2003) 58–62.